

Assessment of pelvic lymph node metastasis in FIGO IB and IIA cervical cancer using quantitative dynamic contrast-enhanced MRI parameters

See Hyung Kim 
Seung Hyun Cho 

PURPOSE

We prospectively determined whether the quantitative parameters derived from dynamic contrast-enhanced magnetic resonance imaging (DCE-MRI) are useful for predicting pelvic lymph node (LN) status in cervical cancer through node-by-node pathologic validation of images.

METHODS

Overall, 182 LNs harvested from 200 consecutive patients with 2018 FIGO stage IB-IIA cervical cancer (82 metastatic and 100 nonmetastatic) were used for node-by-node assessment. Each LN was quantitatively assessed using K^{trans} , V_e , and K_{ep} values. The short-axis diameter, ratio of the long-axis to short-axis diameter, and long-axis diameter were also assessed. Data on metastatic LNs were divided into four groups according to the FIGO staging system. Receiver operating characteristic (ROC) curve analysis was performed to evaluate statistically significant parameters derived from DCE-MRI for the differentiation of metastatic LNs from nonmetastatic LNs.

RESULTS

The mean short-axis diameter of metastatic LNs was significantly larger than that of nonmetastatic LNs (all $P < 0.05$) despite several overlaps. In comparison with nonmetastatic LNs, metastatic LNs showed a significantly lower K^{trans} (all $P < 0.05$); however, K_{ep} and V_e were not significantly different (all $P > 0.05$). For IB3 and IIA2 cervical cancer, K^{trans} had moderate diagnostic ability for differentiating metastatic LNs from nonmetastatic LNs (for IB3: area under the curve [AUC] 0.740, 95% CI 0.657–0.838, 61.7% sensitivity, 80.2% specificity, $P = 0.007$; for IIA2: AUC 0.786, 95% CI 0.650–0.846, 60.2% sensitivity, 81.8% specificity, $P = 0.008$).

CONCLUSION

K^{trans} appears to be a useful parameter for detecting metastatic LNs, especially for IB3 and IIA2 cervical cancer.

Cervical cancer is a major gynecologic malignancy clinically staged according to the recommendations of the International Federation of Obstetrics and Gynecology (FIGO) (1). Lymph node (LN) status plays a vital role in cervical cancer treatment strategies (1, 2). Studies have found that the number of LNs affects the prognosis for patients with cervical cancer (1–3). Some studies of FIGO stage IB to IIA cervical cancer suggest that tumor size may be more effective in predicting LN metastasis (1–4). In addition, the presence of metastatic LNs affects the overall treatment and prognosis in routine practice.

Magnetic resonance imaging (MRI) has been used to assess LN status. Several studies have referred to the size to predict metastatic LNs; however, the proposed cutoff values for differentiating metastatic LNs from nonmetastatic LNs are inconsistent (5–9). Although the size is important for assessing LN status, its value is limited because of overlap between metastatic and nonmetastatic LNs (6–8). Additionally, approximately 50% of metastatic LNs are less than 10 mm in the short-axis diameter (8). For now, the potential of functional imaging in improving diagnostic accuracy has been the focus of recent studies. Examples of functional imaging modalities include diffusion-weighted MRI, ^{18}F -fluorodeoxyglucose positron emission tomography-computed tomography (PET-CT), and LN-specific contrast agent imaging (8, 9); however, these modalities remain challenging for radiologists.

From the Department of Radiology (S.H.K. ✉ kimseehyung72@outlook.kr), Kyungpook National University School of Medicine, Kyungpook National University Hospital, Daegu, Korea; Department of Radiology (S.H.C.), Kyungpook National University School of Medicine, Kyungpook National University Chilgok Hospital, Daegu, Korea.

Received 12 July 2019; revision requested 14 August 2019; last revision received 19 November 2019; accepted 5 December 2019.

Published online 6 July 2020.

DOI 10.5152/dir.2020.19365

You may cite this article as: Kim SH, Cho SH. Assessment of pelvic lymph node metastasis in FIGO IB and IIA cervical cancer using quantitative dynamic contrast-enhanced MRI parameters. *Diagn Interv Radiol* 2020; 26:382–389

Table 1. MRI protocols for imaging sequences

Protocol	TR/TE	Slice thickness (mm)	Number of slices	FOV (mm)	Voxel size (mm)	Number of signals acquired	Scanning time (s)
T2-weighted							
Sagittal	3000/87	3.0	19	180×180	0.7×0.6×0.3	2	150
Coronal	4000/75	3.0	25	220×220	0.7×0.6×0.3	2	172
Transverse	3000/84	3.0	24	180×180	0.6×0.6×0.3	2	198
DCE transverse 3D TWIST	4.83/1.85	3.5	20	250×250	2.0×1.4×3.6	1	324

MRI, magnetic resonance imaging; TR, repetition time; TE, echo time; FOV, field of view; DCE, dynamic contrast-enhanced; 3D TWIST, three-dimensional time-resolved imaging with interleaved stochastic trajectories.

Isolated cancer cells and micrometastases in metastatic LNs may induce physiologic changes before morphologic changes are apparent. For example, the microcirculation is altered when tumor cells invade the microvessels of a small LN; however, its size remains normal. Dynamic contrast-enhanced (DCE)-MRI is a relatively new imaging method that can measure changes in the tissue microvasculature caused by cancer angiogenesis. The influx volume transfer coefficient K^{trans} represents the transendothelial transport of contrast material from the vascular compartment to the tumor interstitium. The efflux volume transfer coefficient K_{ep} represents the transport of contrast material from the tumor interstitium back to the vascular space. The most commonly used DCE-MRI parameter is the volume transfer constant (K^{trans}). The extravascular extracellular leakage volume fraction ($V_e = K^{trans}/K_{ep}$) mainly reflects the percentage of contrast agent in the extravascular extracellular space (10).

The purpose of our study was to prospectively determine whether quantitative parameters derived from DCE-MRI are useful for predicting pelvic LN status in cervical cancer through node-by-node pathologic validation of images.

Main points

- The mean short-axis diameter of metastatic lymph nodes (LNs) were significantly larger than those of nonmetastatic LNs in IB and IIA cervical cancer.
- Metastatic LNs had a lower K^{trans} than nonmetastatic LNs. K_{ep} and V_e parameters were not significantly different between the metastatic and nonmetastatic LNs.
- K^{trans} appears to be a useful parameter for detecting metastatic LNs in case of difficulty to determine LN status using only short-axis diameter, especially for IB3 and IIA2 cervical cancer.

Methods

Patients

Our study was approved by the institutional review board (Protocol Number: KNUH-19-00105), and informed consent was obtained. A total of 230 consecutive patients with 2018 FIGO stage IB-IIA cervical cancer, regardless of the LN status, were included.

All patients underwent laparoscopic surgery between 1 February 2016 and 31 December 2018 to receive radical hysterectomy and pelvic/para-aortic lymphadenectomy as the primary treatment. After biopsy or loop electrosurgical excision procedure (LEEP) confirmation, all patients underwent MRI. A total of 21 patients with serious motion artifacts due to hip movements and 9 patients with metal artifacts caused by titanium clips in the sigmoid colon or rectum were excluded. Finally, our study included 200 patients (age range, 35–68 years; median, 48.5 years). The mean time between MRI and surgery was 10 days (range, 2–21 days).

MRI protocol

MRI was performed using a 3 Tesla MRI System (Skyra, Siemens Healthineers) with a 16-channel phased-array body surface coil. To reduce intestinal peristalsis or rectal spasm, 20 mg of Buscopan (Boehringer Ingelheim) was injected intramuscularly 10–15 min before MRI unless contraindicated.

Tri-planar T2-weighted turbo spin-echo images of the entire pelvic region were obtained. Then, DCE-MRI was performed using a three-dimensional (3D) dynamic transverse T1-weighted sequence at a high spatial and temporal resolution based on time-resolved imaging with interleaved stochastic trajectories (TWIST) sequence that covers the entire pelvic cavity in consecutive sections. The temporal resolution of this sequence was approximately

4.0 ms, and the total acquisition time was 4 min 40 s. The contrast material (0.2 mL/kg gadobutrol) (Gadovist, Bayer Schering Pharma) was administered using a power injector (Medrad Spectris Solaris EP MR Injection System, Bayer Medical Care Inc.) followed by a 20 mL saline flush injection at a flow rate of 2.5 mL/s through the cubital vein. Table 1 shows the parameters of all MRI protocols.

Classification of pelvic LN regions

Five expert gynecologic surgeons performed all the operations and examined the images before lymphadenectomy. An understanding of the location of LN groups in the pelvis is essential for formulating an effective search strategy to determine MRI staging. It is also necessary to accurately describe the detected abnormal LNs to facilitate accurate staging in a standardized manner. The major groups of pelvic LNs may be described as follows: common iliac, internal iliac, external iliac, and obturator chains.

Pathologic assessment

The pathology of LN specimens was evaluated in a standardized manner. First, the specimen was opened at the 12:00 o'clock position, the size of the mass was determined based on three orthogonal diameters by pathologic examination. Next, lymphadenectomy was performed by removing the LN-bearing tissues surrounding the iliac vessels as well as within the obturator fossa superior to the obturator nerve. The LNs were completely processed to a size of 3 mm in the short-axis diameter. LNs were also completely processed in the longitudinal direction. Each LN was sliced at 2 mm intervals perpendicular to the longest diameter to maximize the likelihood of detecting micrometastases. The total number of LNs harvested in each region was recorded.

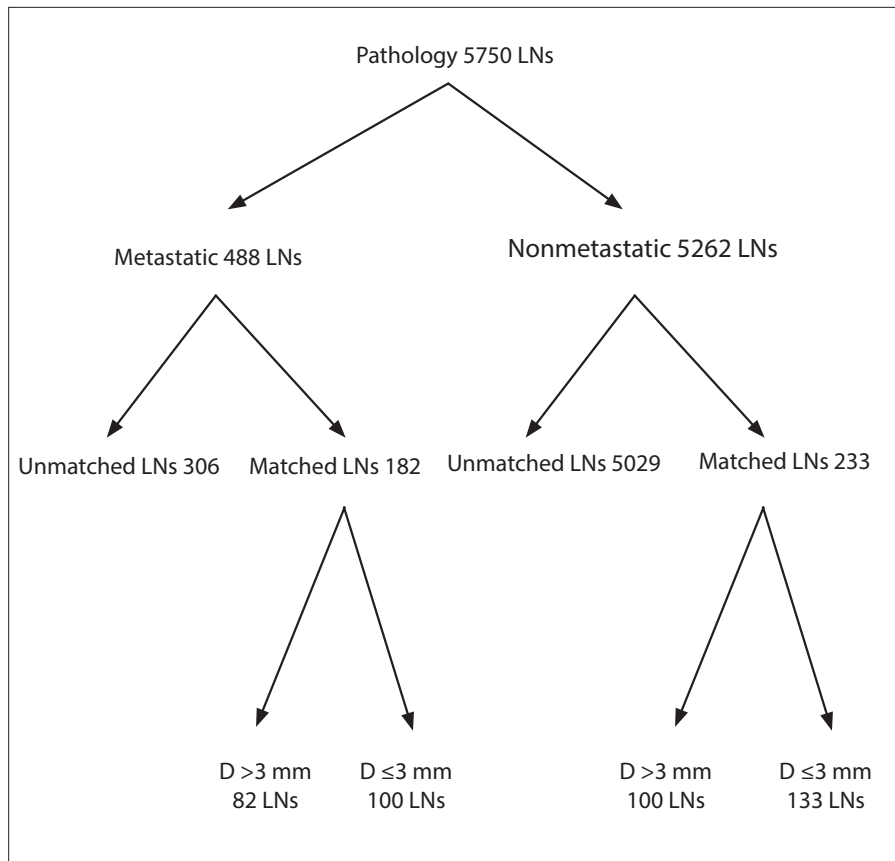


Figure 1. Flowchart of the identification of lymph nodes in dynamic contrast-enhanced magnetic resonance imaging (DCE-MRI) and pathologic assessment. LN, lymph node; D, short-axis diameter.

Image processing and analysis

All images were reviewed and analyzed on a postprocessing multimodality workplace (Syngo VE40A, Siemens Healthineers). Voxelwise MRI signal enhancement time curves were fitted according to a pharmacokinetic model using Tissue 4D software (Siemens Healthineers). First, motion correction was performed for DCE images. Each visible LN region was then postprocessed in the field of view (FOV) of the DCE images by an experienced radiologist who was unaware of the histopathologic results.

In the postprocessing procedure, one region of interest (ROI) was drawn on the widest cross-section of a node, excluding visible necrosis and vessels. T1-weighted signal enhancement was converted to a tracer concentration using the proton density signal. A general arterial plasma concentration-time curve was assumed. Arterial input functions (AIFs) were tested to choose the best one with the smallest chi-square value. Pharmacokinetic parameters were estimated by fitting the Tofts model driven by the AIF (11, 12). The quantitative parameters calculated were K^{trans} (forward volume

transfer constant), K_{ep} (plasma space), and V_e (fraction of extravascular extracellular space volume). The entire nodal volume was included by drawing ROIs for each individual slice, and the AIF of the widest cross-section was used in all ROIs of a node to calculate the mean parameter values.

Subsequently, transverse T2-weighted images were used to investigate the short-axis diameter, ratio of the long-axis to short-axis diameter, and long-axis diameter. LN diameters were measured using electronic calipers with a PACS monitor. Then, the LN positions on the DCE images were confirmed by an expert surgeon with expertise in cervical cancer and the radiologist who performed the postprocessing evaluation. Regional LNs that were visible in the FOV of preoperative DCE images were divided into the four groups mentioned previously. According to the agreed LN positions, the expert surgeon successively localized, removed, and numbered regional LNs one by one in different groups during the procedure. The LNs were then taken to the pathology department and promptly placed in individual trays. All nodes were fixed in formalin and stained

with hematoxylin and eosin (H-E). Thereafter, a pathologist analyzed and classified each node as metastatic or nonmetastatic.

To ensure that a sufficient number of LNs were examined, other LNs that were not identified on DCE images were also harvested from the specimen and pathologically examined. According to pathology, the radiologist matched the LNs with LNs identified in DCE-MRI in the corresponding group, and the LNs were excluded if matching failed. To provide an accurate node-by-node comparison of MRI findings and histopathologic findings, we focused special attention on the nodal size and morphology in addition to the position of the LNs relative to the tumor, ovary, vessels, and adjacent LNs. Only LNs with a short-axis diameter smaller than 3 mm, which are not suitable for quantitative parameter analysis, were excluded in this study.

Statistical analysis

A Shapiro-Wilk test was used to determine the normal distribution of the quantitative data. Normally distributed quantitative data were expressed as mean \pm standard deviation, and non-normally distributed data were expressed as median with interquartile range (IQR). An independent-samples t-test was conducted for normally distributed data to determine the significance of differences and the Mann-Whitney U test was conducted for non-normally distributed data.

Receiver operating characteristic (ROC) curve analysis was performed for statistically significant parameters derived from DCE-MRI, and the area under the ROC curve (AUC) and 95% confidence interval (CI) were calculated. An AUC value <0.5 indicated no diagnostic performance, $0.5\text{--}0.7$ indicated poor performance, $0.7\text{--}0.9$ indicated moderate performance, and >0.9 indicated excellent performance. Each cutoff value was determined to accommodate the best diagnostic accuracy according to the Youden index.

The clinical and pathologic findings were also compared between patients with metastatic LNs and those with nonmetastatic LNs using chi-square or Fisher's exact tests. Statistical analysis was performed with SPSS (version 23.0; SPSS Inc.). A P value <0.05 was considered statistically significant.

Results

The clinical and pathologic findings of the primary tumor and LN status are shown

Table 2. Clinical and pathologic findings of the primary tumor and LN status in 200 patients

Parameter	Total (n=200)	Metastatic LN (n=77)	Nonmetastatic LN (n=123)	P
Age (years)	48.6±9.5	45.2±8.6	50.1±7.3	0.036
Pathologic condition, n (%)				0.475
Squamous cell carcinoma	175 (87.5)	69 (89.6)	106 (86.1)	
Non-squamous cell carcinoma	25 (12.5)	8 (10.4)	17 (13.9)	
Pathologic grade*				< 0.001
Well differentiated	118 (67.4)	30 (43.4)	88 (83.0)	
Moderately differentiated	38 (21.7)	23 (33.3)	15 (14.1)	
Poorly differentiated	19 (10.9)	16 (23.3)	3 (2.9)	
Primary tumor size (mm)	28.6±10.6	35.8±7.9	15.6±4.2	< 0.001
Number of harvested LNs per patient	25.5±14.8	26.6±8.8	24.3±9.9	0.262
2018 FIGO staging, n (%)				< 0.001
IB1	25 (12.5)	5 (12.4)	20 (16.2)	
IB2	74 (37.0)	12 (14.6)	62 (50.4)	
IB3	49 (24.5)	24 (29.2)	25 (20.3)	
IIA1	32 (16.0)	21 (25.6)	11 (8.9)	
IIA2	20 (10.0)	15 (18.2)	5 (4.2)	

Values are presented as mean ± standard deviation or n (%).

LN, lymph node; FIGO, International Federation of Obstetrics and Gynecology.

*Pathologic grade is included for 175 patients with only squamous cell carcinoma.

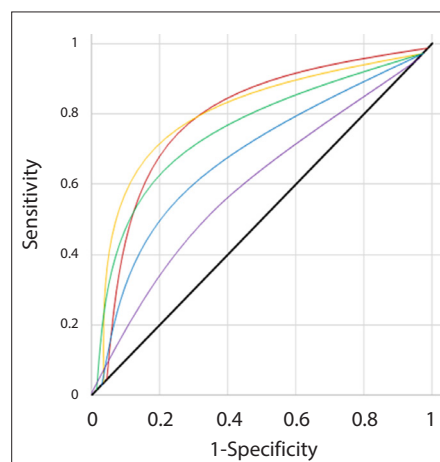


Figure 2. Receiver operating characteristic (ROC) curves and area under the receiver operating characteristic curves (AUCs) for determining lymph node status using forward volume transfer constant (K^{trans}) values. IB1, purple line; IB2, green line; IB3, red line; IIA1, blue line; IIA2, orange line.

in Table 2. Most patients were in FIGO stage IB2–IB3 (61.5%). A total of 175 patients had squamous cell carcinoma (87.5%), with well-differentiated cells in 118 patients (67.4%). Patients with rare or other pathology included 2 patients with small cell carcinoma and 1 patient with undifferentiated carcinoma. The mean tumor size was 28.6 mm.

A total of 5750 LNs were harvested from the hysterectomy specimens of 200 patients, with an average of 25.6 LNs per patient. A total of 488 LNs from 92 patients were metastatic, and 5262 LNs were not metastatic. For node-by-node assessment, 415 LNs identified in pathologic evaluation were matched exactly with LNs identified in DCE-MRI, while the remaining 5335 LNs were not matched. Among the 415 matched LNs, 233 LNs with a short-axis diameter smaller than 3 mm were excluded, and the remaining 182 LNs (82 metastatic and 100 nonmetastatic) were used for the final assessment. Fig. 1 shows a flowchart of the identification of LNs in DCE-MRI and pathologic assessment. There were 77 metastatic LNs in the internal iliac, 54 in the external iliac, 26 in the common iliac, and 25 in the obturator chains.

The quantitative parameters of LNs identified in DCE-MRI and morphologic evaluation are shown in Table 3. The short-axis diameter of metastatic LNs (median, 11.8 mm; IQR, 3.9 mm) was significantly larger than that of nonmetastatic LNs (median, 8.1; mm IQR, 3.6 mm) in IB and IIA cervical cancer (all $P < 0.05$). Nevertheless, there were many overlaps between metastatic and nonmetastatic LNs. The ratio of the long-axis to short-axis diameter and long-axis diameter were similar between metastatic and nonmetastatic LNs.

In comparison with nonmetastatic LNs, metastatic LNs showed a significantly lower K^{trans} in IB and IIA cervical cancer. These differences were significant in IB3 and IIA2 cervical cancer. Differences in K_{ep} and V_e between metastatic and nonmetastatic LNs were not statistically significant (all $P > 0.05$). Fig. 2 shows the ROC curves and relative values for IB and IIA cervical cancer. For IB3 and IIA2 cervical cancer, K^{trans} had moderate diagnostic ability for differentiating metastatic LNs from nonmetastatic LNs (for IB3: AUC 0.740, 95% CI 0.657–0.838, $P = 0.007$; for IIA2: AUC 0.786, 95% CI 0.650–0.846, $P = 0.008$), with cut-off values of 0.081 min^{-1} (61.7% sensitivity, 80.2% specificity) and 0.085 min^{-1} (60.2% sensitivity, 81.8% specificity), respectively. For IB1, IB2, and IIA1 cervical cancer, K^{trans} had poor diagnostic ability for distinguishing metastatic LNs from nonmetastatic LNs (for IB1: AUC 0.618, 95% CI 0.523–0.649, $P = 0.011$, with 0.069 min^{-1} cutoff value, 64.1% sensitivity, 70.9% specificity; for IB2: AUC 0.679, 95% CI 0.592–0.754, $P = 0.009$, with 0.076 min^{-1} cutoff value, 62.8% sensitivity, 75.2% specificity; for IIA1: AUC 0.642, 95% CI 0.551–0.662, $P = 0.011$, with 0.071 min^{-1} cutoff value, 64.3% sensitivity, 73.9% specificity). Figs. 3 and 4 show representative results.

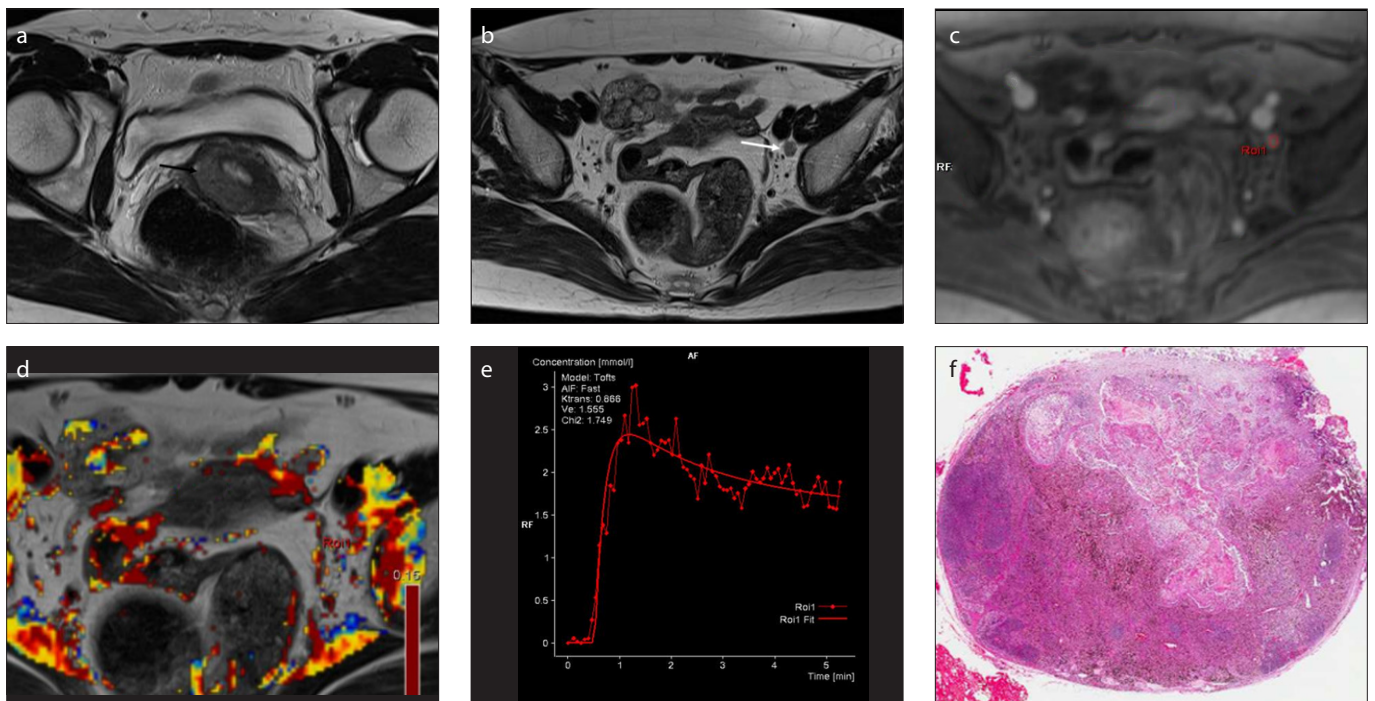


Figure 3. a–f. A 57-year-old patient with FIGO IB3 cervical cancer. T2-weighted images (a, b) show mass (black arrow) and lymph node (white arrow, short-axis diameter 8 mm) in left external iliac chain. DCE image (c) shows ROI 1 (red circle) placed at the widest cross section of the regional lymph node. Panel (d) shows the K^{trans} parametric map and estimated DCE-MRI parameters ($K^{\text{trans}} = 0.003$, $K_{\text{ep}} = 0.37$, and $V_e = 0.032$). An arterial plasma concentration-time curve was assumed, and the best arterial input function (AIF) was used to fit the curve (e). Photomicrograph (f) shows metastatic squamous cell carcinoma lesions in the lymph node (H-E, $\times 40$).

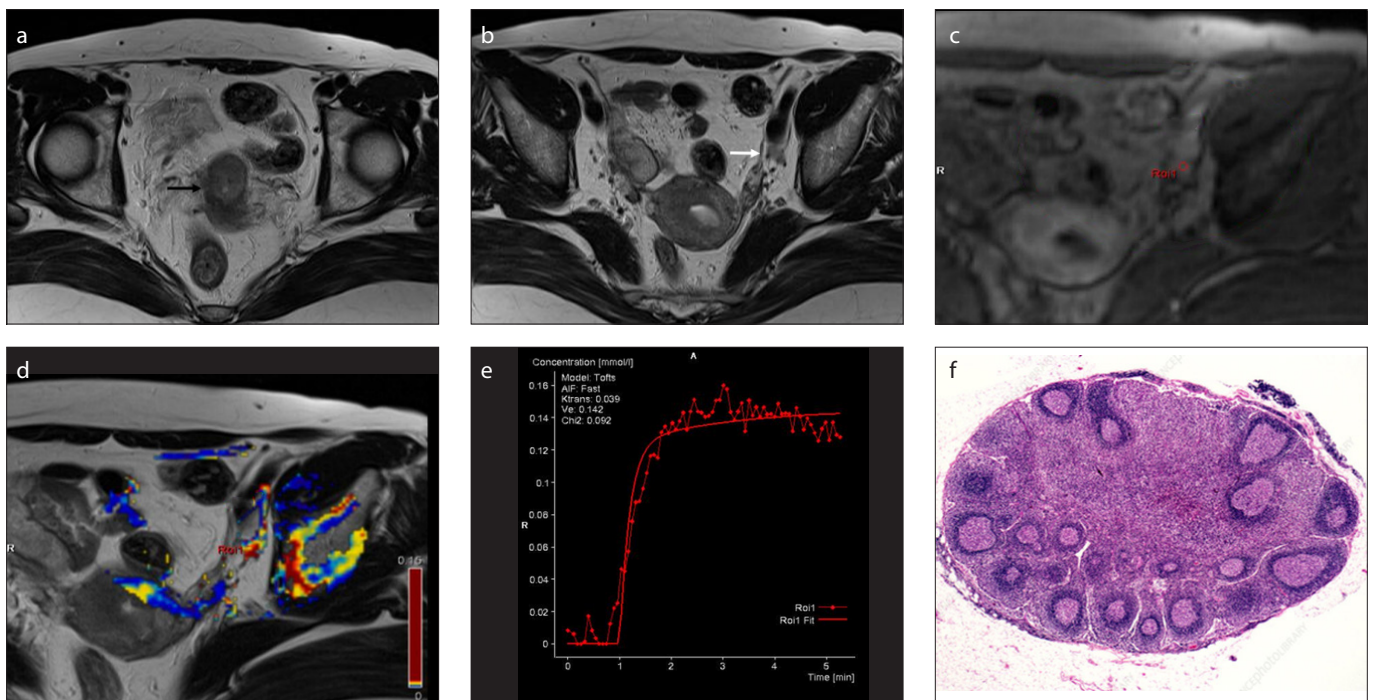


Figure 4. a–f. A 55-year-old patient with FIGO IB2 cervical cancer. T2-weighted images (a, b) show a mass (black arrow) and lymph node (white arrow, short-axis diameter 10 mm) in the left external iliac chain. DCE image (c) shows ROI 2 (red circle) placed at the widest cross-section of the regional lymph node. Panel (d) shows the K^{trans} parametric map generated and DCE-MRI parameters estimated ($K^{\text{trans}} = 0.015$, $K_{\text{ep}} = 0.33$, and $V_e = 0.036$). An arterial plasma concentration-time curve was assumed, and the best arterial input function (AIF) was used to fit the curve (e). Photomicrograph (f) shows no metastatic lesion in the lymph node (H-E, $\times 40$).

Discussion

Our results demonstrated that the K^{trans} of metastatic LNs was lower than that of non-metastatic LNs in IB and IIA cervical cancer; however, K_{ep} and V_e did not show significant differences. Specifically, when the tumor size was large, e.g., stage IB3 and IIA2, the diagnostic efficacy was better. K^{trans} and K_{ep} are quantitative values of the blood flow and permeability between the cancer interstitial space and the vascular compartment (13). K^{trans} represents the contrast agent influx rate from the plasma to the interstitial space. It is increased in tissues with rich blood flow, high vascular permeability, or a large permeable surface. On the other hand, K_{ep} has a positive correlation with vascular permeability, representing the reflux flow rate of the contrast material from the interstitial space to the plasma. Abnormal angiogenesis in cancer tissues can increase microvessel density resulting from leakage, twisted shape, and vessel wall expansion (14–16). Therefore, we hypothesized that the microcirculation of metastatic LNs in cervical cancer may be decreased.

Morphologic MRI is suitable for LN studies because it provides high-resolution images (3). In other studies using the short-axis diameter as the cutoff for determining LN status, metastatic LNs were larger than nonmetastatic LNs. Diameter limits ranging from 6 to 15 mm were used, with 10 mm being the most common cutoff value for the upper limit of nonmetastatic LNs (3–5). In another study, a short-axis diameter of 9 mm was the cutoff value on MRI on a region-by-region basis as well as a node-by-node basis (7). The ratio of the long-axis to short-axis diameter and long-axis diameter are unclear in most studies, and several studies have reported accuracy rates of 60%–70% using the ratio of the long-axis to short-axis diameter and long-axis diameter in MRI (5–8). In our study, analysis using the ratio of the long-axis to short-axis diameter and long-axis diameter revealed nonsignificant differences between metastatic LNs and nonmetastatic LNs. It is possible that the cross-section in the transverse image is not accurately representative of the largest cross-section of the LN.

DCE-MRI can be used to noninvasively assess tissue microcirculatory function. The visibility of the contrast material passing through the capillary bed is associated with its formation temporarily in the blood vessel space before it quickly passes to the

Table 3. Quantitative parameters of 182 LNs identified in DCE-MRI and morphologic evaluation according to the 2018 FIGO staging system

Parameter	Metastatic LN	Nonmetastatic LN	t/Z	P
IB1 (n=18), n (%)	8 (10.0)	10 (10.0)		
K^{trans}	0.011±0.003	0.014±0.004 ^a	3.459	0.011
K_{ep}	0.30 (0.12)	0.32 (0.15) ^b	-1.482	0.135
V_e	0.024 (0.015)	0.028 (0.019) ^b	-1.072	0.268
Short-axis diameter (mm)	11.7 (2.5)	7.3 (3.6) ^b	1.241	0.027
Ratio of long- to short-axis diameter	1.29±0.12	1.59±0.08 ^a	0.538	0.275
Long-axis diameter (mm)	12.1±3.4	11.8±3.2 ^a	3.452	0.091
IB2 (n=40), n (%)	17 (20.7)	23 (23.0)		
K^{trans}	0.008±0.003	0.012±0.006 ^a	3.182	0.009
K_{ep}	0.42 (0.15)	0.30 (0.17) ^b	-1.786	0.267
V_e	0.022 (0.017)	0.034 (0.021) ^b	-1.187	0.298
Short-axis diameter (mm)	11.3 (3.4)	7.8 (4.3) ^b	1.231	0.027
Ratio of long- to short-axis diameter	1.09±0.09	1.37±0.05 ^a	0.527	0.387
Long-axis diameter (mm)	12.4±3.4	11.5±3.8 ^a	3.112	0.073
IB3 (n=68), n (%)	32 (39.0)	36 (36.0)		
K^{trans}	0.005±0.002	0.012±0.005 ^a	3.647	0.007
K_{ep}	0.35 (0.12)	0.37 (0.15) ^b	-1.685	0.248
V_e	0.026 (0.14)	0.031 (0.19) ^b	-1.173	0.296
Short-axis diameter (mm)	9.5 (3.0)	8.2 (4.2) ^b	1.412	0.039
Ratio of long- to short-axis diameter	1.13±0.07	1.52±0.09 ^a	0.627	0.433
Long-axis diameter (mm)	11.5±3.4	10.9±2.8 ^a	3.262	0.067
IIA1 (n=32), n (%)	15 (18.2)	17 (17.0)		
K^{trans}	0.009±0.004	0.012±0.009 ^a	3.051	0.011
K_{ep}	0.46 (0.18)	0.43 (0.21) ^b	-1.546	0.248
V_e	0.033 (0.014)	0.039 (0.27) ^b	-1.142	0.286
Short-axis diameter (mm)	10.1 (3.7)	8.3 (4.5) ^b	1.212	0.031
Ratio of long- to short-axis diameter	1.07±0.07	1.62±0.05 ^a	0.497	0.356
Long-axis diameter (mm)	12.9±3.7	10.7±3.0 ^a	3.012	0.061
IIA2 (n=24), n (%)	10 (12.1)	14 (14.0)		
K^{trans}	0.006±0.003	0.013±0.004 ^a	3.537	0.008
K_{ep}	0.39 (0.15)	0.031 (0.17) ^b	-1.627	0.239
V_e	0.023 (0.019)	0.028 (0.016) ^b	-1.171	0.278
Short-axis diameter (mm)	9.2 (3.8)	7.9 (3.4) ^b	1.309	0.035
Ratio of long- to short-axis diameter	10.4±0.06	1.56±0.07 ^a	0.615	0.421
Long axis diameter (mm)	11.9±2.7	10.6±3.1 ^a	3.187	0.061

Values are presented as mean ± standard deviation or median (interquartile range) unless otherwise noted. LN, lymph node; DCE-MRI, dynamic contrast-enhanced magnetic resonance imaging; FIGO, International Federation of Obstetrics and Gynecology; t/Z, t test/Mann-Whitney U test; K^{trans} , forward volume transfer constant; K_{ep} , plasma space; V_e , fraction of extravascular extracellular space volume.
^aStudent t test. ^bMann-Whitney U test.

extravascular space at a rate determined by the permeability of microvessels, their surface area, and blood flow. Contrast material distribution is repeatedly measured in DCE-MRI to assess *in vivo* LN microcirculation and quantitatively distinguish metastatic and nonmetastatic LNs (17). Microvessel density has been found to be an independent predictor of metastatic LNs (18). Generally, arterioles carry blood to a nonmetastatic LN, and the contrast agent enters the interstitial space from the plasma through the capillary networks of the LN. However, once cancer tissues replace the capillaries of a nonmetastatic LN, the blood flow changes. Although cancer tissues can occupy an area of the capillaries in LNs, the blood flow to these LNs is not completely impeded (19). In this environment, metastatic LNs have a significantly longer time-to-peak, lower peak enhancement, lower maximum slope, and slower washout pattern in a contrast-enhanced time-intensity curve. Accordingly, the percentage of continuous enhancing voxels in metastatic LNs has been reported to be significantly higher than in nonmetastatic LNs. Additionally, metastatic LNs exhibited a lower signal-intensity ratio derived before and after contrast agent administration, indicating mild enhancement (20–22). Our results for K^{trans} were similar to those of previous studies showing that blood flow was reduced in metastatic LNs (23, 24). The heterogeneous enhancement of LNs could be attributed to cancer infiltration, necrosis, or mucin pools; however, in our study, quantitative enhancement pattern analysis was not used to differentiate metastatic LNs from nonmetastatic LNs. Vessel regression resulted in necrosis in the central part of the cancer area; however, angiogenesis was initiated at the cancer margin, supporting cancer survival and further growth. Therefore, cancer vessels may be present at the metastatic LN margin when cancer proliferation enlarges the LN size (22). Unlike our imaging processing, the parameters were calculated only from the widest cross-section of an LN rather than the entire LN volume. If the ROI placed at the widest cross-section of a metastatic LN contained some tumor vessels, blood flow and K^{trans} would be increased. Therefore, the K^{trans} derived from one ROI could be affected by the pathologic heterogeneity of the metastatic LN and does not exactly reflect the blood flow. Our study showed no significant difference in the V_e between metastatic and nonmetastatic LNs. This may be explained

by the different metastatic stages of the LNs. In the early stage, the proliferation of cancer cells is predominant over metastatic LN necrosis. Cancer cell proliferation gradually enlarges the size of metastatic LNs. Because of the decreased blood flow, micronecrosis occurs, increasing the interstitial space. Under these conditions, the V_e may differ between metastatic and nonmetastatic LNs.

Our study has several limitations. First, some assumptions have been made in the node-by-node comparison. Determining the pathology of individual LNs identified on MRI remains challenging. We proposed a histogram analysis method for analyzing the mean, standard deviation (SD), coefficient of variation (CV), kurtosis, skewness, IQR, and percentile of DCE-MRI. Different histogram parameters for efficiently distinguishing between metastatic and nonmetastatic tissues would be applied in the LNs. The second limitation is that although the K^{trans} values and short-axis diameter are useful for MRI, metastatic and nonmetastatic LNs overlap significantly in this region. The third limitation is the small number of included LNs, which may weaken the statistical results. Finally, we used Tissue 4D software to calculate the DCE-MRI parameters, which could affect the reproducibility of our study at institutions where the software is not used. Nevertheless, to our knowledge, this is the first study to demonstrate that DCE-MRI parameters could determine LN status according to the tumor size.

In conclusion, K^{trans} appears to be a useful parameter for detecting metastatic LNs when it is difficult to determine LN status using only the short-axis diameter on MRI, especially for IB3 and IIA2 cervical cancer.

Conflict of interest disclosure

The authors declared no conflicts of interest.

References

1. Parkin DM, Bray F, Ferlay J, Pisani P. Estimating the world cancer burden: Globocan 2000. *Int J Cancer* 2001; 94:153–156. [Crossref]
2. Ballon SC, Berman ML, Lagasse LD, Petrilli ES, Castaldo TW. Survival after extraperitoneal pelvic and paraaortic lymphadenectomy and radiation therapy in cervical carcinoma. *Obstet Gynecol* 1981; 57:90–95.
3. Averette HE, Dudan RC, Ford JH Jr. Exploratory celiotomy for surgical staging of cervical cancer. *Am J Obstet Gynecol* 1972; 113:1090–1096. [Crossref]
4. Hawnaur JM, Johnson RJ, Buckley CH, Tindall V, Isherwood I. Staging, volume estimation and assessment of nodal status in carcinoma of the cervix: comparison of magnetic resonance imaging with surgical findings. *Clin Radiol* 1994; 49:443–452. [Crossref]
5. Hricak H, Quivey JM, Campos Z, et al. Carcinoma of the cervix: predictive value of clinical and magnetic resonance (MR) imaging assessment of prognostic factors. *Int J Radiat Oncol Biol Phys* 1993; 27:791–801. [Crossref]
6. Reinhardt MJ, Ehrhrt-Braun C, Vogelgesang D, et al. Metastatic lymph nodes in patients with cervical cancer: detection with MRI and FDG PET. *Radiology* 2001; 218:776–782. [Crossref]
7. Sironi S, Buda A, Picchio M, et al. Lymph node metastasis in patients with clinical early-stage cervical cancer: detection with integrated FDG PET/CT. *Radiology* 2006; 238:272–298. [Crossref]
8. Williams AD, Cousins C, Soutter WP, et al. Detection of pelvic lymph node metastases in gynecologic malignancy: a comparison of CT MRI, and positron emission tomography. *AJR Am J Roentgenol* 2001; 177:343–348. [Crossref]
9. Kwee TC, Basu S, Torigan DA, Saboury B, Alavi A. Defining the role of modern imaging techniques in assessing lymph nodes for metastasis in cancer: evolving contribution of PET in this setting. *Eur J Nucl Med Mol Imaging* 2011; 38:1353–1366. [Crossref]
10. Huang W, Tudorica LA, Li X, et al. Discrimination of benign and malignant breast lesions by using shutter-speed dynamic contrast-enhanced MRI. *Radiology* 2011; 261:394–403. [Crossref]
11. Tofts PS, Brix G, Buckley DL, et al. Estimating kinetic parameters from dynamic contrast-enhanced T1-weighted MRI of a diffusible tracer: standardized quantities and symbols. *J Magn Reson Imaging* 1999; 10:223–232.
12. Brix G, Semmler W, Port R, Schad LR, Layer G, Lorenz WJ. Pharmacokinetic parameters in CNS Gd-DTPA enhanced MRI. *J Comput Assist Tomogr* 1991; 15:621–628. [Crossref]
13. Hylton N. Dynamic contrast-enhanced magnetic resonance imaging as an imaging biomarker. *J Clin Oncol* 2006; 24:3293–3298. [Crossref]
14. Bergers G, Benjamin LE. Tumorigenesis and the angiogenic switch. *Nat Rev Cancer* 2003; 3:401–410. [Crossref]
15. Vag T, Slotta-Huspenina J, Rosenberg R, et al. Computerized analysis of enhancement kinetics for preoperative lymph node staging in rectal cancer using dynamic contrast-enhanced magnetic resonance imaging. *Clin Imaging* 2014; 38:845–849. [Crossref]
16. Yu XP, Wen L, Hou J, et al. Discrimination between metastatic and nonmetastatic mesorectal lymph nodes in rectal cancer using intravoxel incoherent motion diffusion-weighted magnetic resonance imaging. *Acad Radiol* 2016; 23:479–485. [Crossref]
17. Cui C, Cai H, Liu L, Li L, Tian H, Li L. Quantitative analysis and prediction of regional lymph node status in rectal cancer based on computed tomography imaging. *Eur Radiol* 2011; 21:2318–2325. [Crossref]
18. Holash J, Wiegand SJ, Yancopoulos GD. New model of tumor angiogenesis: dynamic balance between vessel regression and growth mediated by angiopoietins and VEGF. *Oncogene* 1999; 18:5356–5362. [Crossref]
19. Langer DL, van der Kwast TH, Evans AJ, et al. Prostate tissue composition and MR measurements: investigating the relationships between ADC, T2, K_{trans}, V_e, and corresponding histologic features. *Radiology* 2010; 255:485–494. [Crossref]

20. Qian CN, Berghuis B, Tsarfaty G, et al. Preparing the "soil": the primary tumor induces vasculature reorganization in the sentinel lymph node before the arrival of metastatic cancer cells. *Cancer Res* 2006; 66:10365–10376. [\[Crossref\]](#)
21. Paldino MJ, Barboriak DP. Fundamentals of quantitative dynamic contrast-enhanced MRI. *Magn Reson Imaging Clin N Am* 2009; 17:277–289. [\[Crossref\]](#)
22. Türkbey B, Thomasson D, Pang Y, Bernardo M, Choyke PL. The role of dynamic contrast-enhanced MRI in cancer diagnosis and treatment. *Diagn Interv Radiol* 2010; 16:186–192. [\[Crossref\]](#)
23. Choi SH, Moon WK. Contrast-enhanced MRI of lymph nodes in cancer patients. *Korean J Radiol* 2010; 11:383–394. [\[Crossref\]](#)
24. Grøvik E, Redalen KR, Storås TH, et al. Dynamic multi-echo DCE- and DSC-MRI in rectal cancer: Low primary tumor K_{trans} and $\Delta R2^*$ peak are significantly associated with lymph node metastasis. *J Magn Reson Imaging* 2017; 46:194–206. [\[Crossref\]](#)